

Figure 1. A schematic diagram of the model to estimate spectral position on the detector from instrumental temperatures and relative motion of the spacecraft.

The artificial spectral drift amounts to 70 km s^{-1} in Doppler velocity scale and introduces a significant effect on velocity measurements. A commonly used method so far is to assume that a net Doppler shift vanishes in a quiet region. As a quiet region is not always included in the EIS field of view, the assumption of zero net velocity is not always applicable in some cases. It has been reported that the spectrum drift is connected with temperature variations in the spectrometer. Brown *et al.* (2007) showed that the spectral drift is correlated with grating temperature variation. But their relationship is not simple because a slight phase difference is found between them. A qualitative comparison between the spectrum drift and instrumental temperatures shows that the spectral drift reflects all aspects of the temperature variations. Rybák *et al.* (1999) demonstrated that periodic spectral shifts of the SUMER spectrometer can be corrected by using instrumental temperatures. However, a more complex method is needed to reproduce the spectral drifts of the EIS.

Our goal is to develop an empirical model to reproduce spectral drift from instrumental temperatures so that the Doppler velocity can be determined from any spectra obtained with EIS. The organization of the paper is as follows: The scheme of the model and definition of their input and output are described in Section 2. A comparison between the model and the measured spectral position is presented in Section 3. In Section 4, the performance of the model and its application to observations are discussed. The curvatures and spatial offset of the spectrum, which are essential for data analysis with EIS, are described in the Appendices.

2. Method

Figure 1 shows a schematic diagram of the model to reproduce spectral position on the detector from instrumental temperatures. Its input consists of instrumental temperatures of the EIS. The EIS employs 31 temperature sensors which allows measurement of the temperature distribution of the optical bench. They are monitored at 10 s intervals by the instrument. These instrumental temperatures show seasonal variation caused by the variation of the Sun – Earth distance. In addition, some temperatures exhibit short term variation in sync with the orbital revolution of the spacecraft (98 min period), while the rest

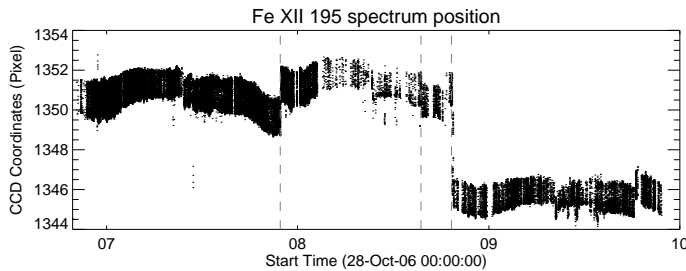


Figure 2. Temporal evolution of spectral position of Fe XII $\lambda 195.12 \text{ \AA}$ on the detector. Vertical dashed lines indicates times of discontinuity in the spectral position.

of temperatures show only seasonal variations. For the short varying group, temperatures at 5 min earlier and later are also incorporated into the model to account for their time derivatives. Temperature sensors placed close to each other are redundant, and are reduced to one temperature to minimize the number of inputs. The total number of inputs for the model is 34.

An artificial neural network (ANN) is employed to deduce spectral drift from the instrumental temperatures. It has been demonstrated that the ANN is an efficient method for solving a complex problem, such as deriving atmospheric parameters from Stokes profiles (Carroll and Staude, 2001; Socas-Navarro, 2003; Borrero *et al.*, 2010). The basics of the ANN are described in Bishop (1995). The ANN is realized as layers of nodes, which is called a feed forward network. Two nodes in neighbouring layers are connected by a link which has a weight and a bias to define a relationship between the nodes. The ANN consists of input layer, hidden layer, and output layer. In our model, the input layer is a set of instrumental temperatures. The hidden layer is a layer of nodes connecting the input and the output. A single hidden layer has been employed to keep the model simple. The output is a single value representing the spectral position under given instrumental temperatures. The ANN is trained to reproduce the relationship between input and output by optimizing weights and biases for the links. The ANN allows us to deduce an empirical relationship between instrumental temperatures and spectral drift from the huge data set.

It is necessary to compensate for the Doppler shift caused by the spacecraft motion relative to the observed object on the Sun. The motion of the spacecraft is calculated onboard to tune the narrow band filter of the Solar Optical Telescope (Tsuneta *et al.*, 2008) on *Hinode*. The relative velocity of the spacecraft consists of the spacecraft revolution, the Sun – Earth distance variation, and solar rotation of the observing region which add up to $\pm 6 \text{ km s}^{-1}$ at the largest. The calculated velocity is retrieved from the spacecraft status data and is added to the output of the ANN to estimate spectral position on the detector (Figure 1).

The output of the model is a spectral center position in Fe XII $\lambda 195.12 \text{ \AA}$. This emission line is one of the EIS core lines, hence is included in all observations. As it is an intense emission line, the spectrum center can be accurately determined in the quiet region as well as in the active region. To minimize the effect of localized flow on the Sun, data obtained with a slit length of 240 arcsec or greater are

selected for this analysis. All EIS data meeting the criteria are retrieved from *Hinode* archive in DARTS (Matsuzaki *et al.*, 2007). A Gaussian fit is applied to the spectrum to determine the center position at each slit height. The instrumental spectral curvature is corrected by subtracting it from the measured spectral center position (see Appendix A for the spectral curvature of the EIS). Then mean spectral position at each exposure is derived from an averaged spectral center position along the slit.

Figure 2 presents a temporal variation of the spectral position for three years since the *Hinode* launch. A short term variation caused by the spacecraft revolution, which is observed throughout the period, amounts to two pixels in peak to peak amplitude. A seasonal variation of the spectral position is primarily due to the variation of Sun – Earth distance in one year cycle. The eclipse season in May – July and heater configuration changes also affect the spectral position. Two noticeable discontinuities in spectral position are found at the time of slit focus adjustment on 24 August 2008 and grating focus adjustment on 21 October 2008, which are marked by dashed lines in Figure 2. A large discontinuity on 29 November 2007, which is indicated by dashed line in Figure 2, is attributed to a heater configuration change.

An ANN was built by using the multilayer perceptron software package provided in the ROOT data analysis framework (Brun and Rademakers, 1997)¹. The package is an open source software written in C++ language. Because the ANN is an empirical method, it is important to prepare a large number of data sets so that they represent all possible conditions of the instrument. To reproduce seasonal variation of the spectral position, the ANN needs to be developed from data set at least for one year.

Series of data are divided at the times of the grating and the slit movements, which changed the optical alignment of the spectrometer. On top of these discontinuities, data are also separated at the heater configuration change on 29 November 2007 because the discontinuity is too large to be reproduced by a single model. Three independent models A, B, and C are developed for the split time series, which are given in the second column of Table 1. No independent model is built between 24 August 2008 and 20 October 2008 because of the small number of samples during that short interval.

The ANN is trained using the back propagation algorithm provided with the multilayer perceptron package of the ROOT. The performance of our model is measured by a residual between measured spectral position and the model output. The major causes of the residual are the error of the ANN and flows on the Sun which are independent of instrumental temperatures. Since we employ a large number of data, velocities of the flows are assumed to be random. Thus, the residual is regarded as the upper limit of the ANN error. In the following section, root mean square (rms) of the residual is used as a measure of the ANN error. The data set for each model is randomly divided into 80% of training group and 20% of test group. In the course of the training, the ANN is trained with the training group, while the performance of ANN is evaluated with the test group. The training process is repeated until the performance reaches a steady state.

¹See also <http://root.cern.ch/>.

Table 1. Parameters for the models

Model	Period	Samples	rms of residual (pixel) (km s ⁻¹)	
A	03 Nov 2006 – 28 Nov 2007	6.5×10^5	0.12	4.0
B	29 Nov 2007 – 23 Aug 2008	9.5×10^4	0.16	5.4
C'	24 Aug 2008 – 20 Oct 2008	1.1×10^4	0.14	4.7
C	21 Oct 2008 – 28 Nov 2009	1.6×10^5	0.15	5.0
	Total	9.2×10^5	0.13	4.4

A byproduct of our work is determination of the offset between the 1'' wide slit and 2'' wide slit of EIS. In principle, spectral drift caused by instrumental temperature variations should work in the same way for both slits. Two independent models are developed for 1'' slit and 2'' slit spectra in the period A. The offset between the 1'' slit and the 2'' slit in the wavelength dimension has been derived from the difference between two models, which is 8.20 in CCD pixels. Spectra recorded with the 1'' slit and the 2'' slit of EIS are merged after compensating for the offset between two slits. To increase the number of data set, the merged data are used for building three ANNs. The composite numbers of 1'' data and 2'' data are presented in the third column of Table 1.

Finally, the gap between the model B and C is filled by extending the model C, assuming that the grating adjustment on 21 October 2008 produced only a constant offset in spectral position. The spectral positions between 24 August 2008 and 21 October 2008 are reproduced the best when the model C is shifted by 4.88 pixel. For this period, a modified model C' is composed by adding a constant offset of 4.88 pixel to model C.

3. Results

3.1. Performance of the Model

Table 1 presents the parameters for the developed models. The last two columns are the rms of the residuals, which are difference between the measured spectral position and the model estimation. The residual spectral shift is also converted to Doppler velocity at Fe XII $\lambda 195.12$ Å. Model A, which is created from the largest number of samples gives the lowest residual. The performance of model B is worse than the others, which is probably due to a small number of samples and its period falling short of one year. Model C', which is built by shifting model C, gives a similar residual to the other models. The last row of Table 1 presents the overall performance of the composite model. The composite model reproduces the spectral drift of the EIS with a moderate accuracy of 4.4 km s⁻¹ all through the period.

Figure 3 shows distributions of the residual for the three models. Vertical dashed lines in each plot mark the rms of the residual, which are also presented

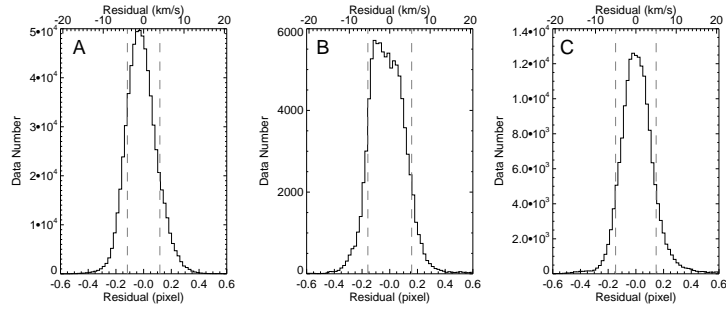


Figure 3. Distributions of the residuals for the three models. Dashed lines indicate the rms of the residuals.

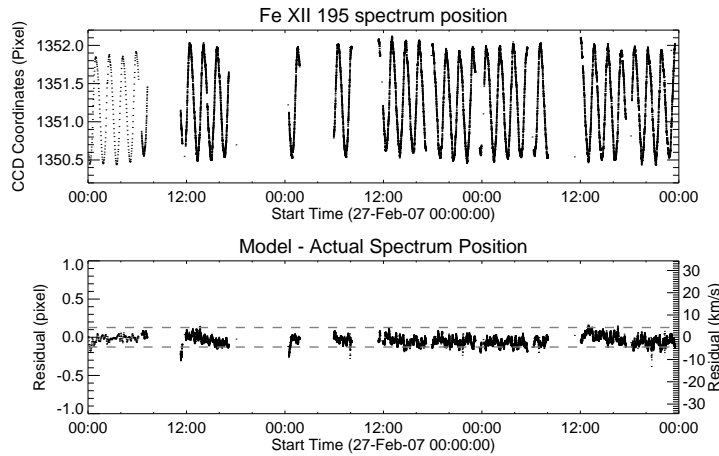


Figure 4. Top: Temporal evolution of spectral position Fe XII $\lambda 195.12$ Å in CCD pixel coordinates. Bottom: difference between the model estimation and measured spectral positions in unit of pixel coordinate. Right vertical axis indicates Doppler velocity scale. Dashed lines indicates $\pm 1\sigma$ levels of the residual, which is ± 0.13 pixel.

in Table 1. The distributions show that the majority of the residuals fall within the rms ranges, but the residuals have greater values in some cases.

Figure 4 presents a time series of measured spectral positions and residuals in a day period, when the spacecraft does not experience an eclipse. The spectral position exhibits sinusoidal variation with the orbital period of the spacecraft, which amounts to 1.5 pixels in peak to peak amplitude. In the bottom plot, the residuals are virtually suppressed below ± 0.13 pixel range, which means that the model reproduces the sinusoidal variation caused by instrumental temperatures quite well.

Figure 5 presents a time series in an eclipse period, when the spacecraft experiences an eclipse in each orbital revolution. The variation of spectral position is no longer sinusoidal but a peculiar curve with a large amplitude of two pixels. This is primarily because the EIS instrument experiences large temperature variation in the day – night cycle of the spacecraft. But the residuals in the lower plot still

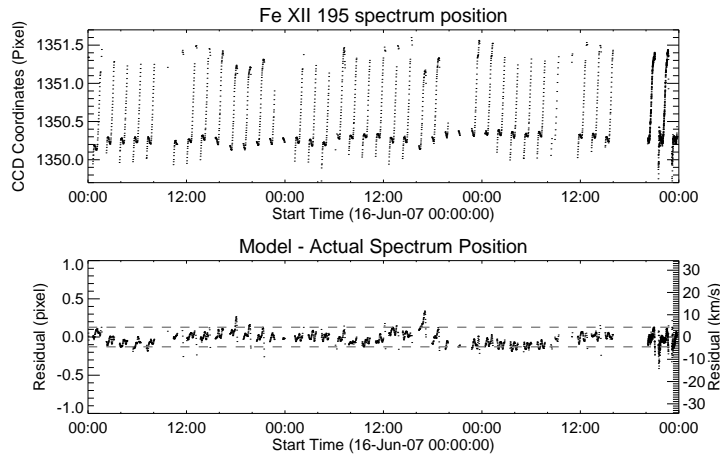


Figure 5. The same as Figure 4 but for an eclipse period.

remain at the same level as the day period, which demonstrates that the model can also work in an eclipse period.

3.2. Comparison with Other Correction Methods

Figure 6 shows coronal loops observed after a flare on 17 December 2006 which was studied by Hara *et al.* (2008). Figure 6b shows the Doppler velocity after applying the correction method developed in the present paper. The velocity averaged at each exposure is plotted in Figure 6c by solid line. For comparison, velocity derived from a cubic spline fit to the spectral drift, which is implemented in the `eis_orbit_spline` procedure in the EIS tree of Solar Software², is also presented in Figure 6d.

A major difference between the two methods is that the spline fit method, which has been commonly used for velocity measurement, assumes the mean velocity in the observed field should be zero, while our method does not assume that. Our model estimates spectral drift only from instrumental temperatures and relative motion of the spacecraft. Averaged velocities plotted in Figure 6c characterize two methods; the velocity determined by spline fitting (dotted line) exhibits zero velocity all through the raster scan, while the average velocity processed by our method (solid line) deviates from zero. However, the assumption of zero velocity might not be valid in active regions, where localized high speed flows are commonly detected. One of major advantages of our method is that the resultant velocity is not affected by an average velocity in the observing field.

3.3. Extending the Method to Other Wavelengths

Although this correction method is developed for the Fe XII $\lambda 195.12 \text{ \AA}$ emission line, the instrumental drift of the spectrum should also work in the same way for

²Solar Software (SSW) is available at <http://www.lmsal.com/solarsoft/>.

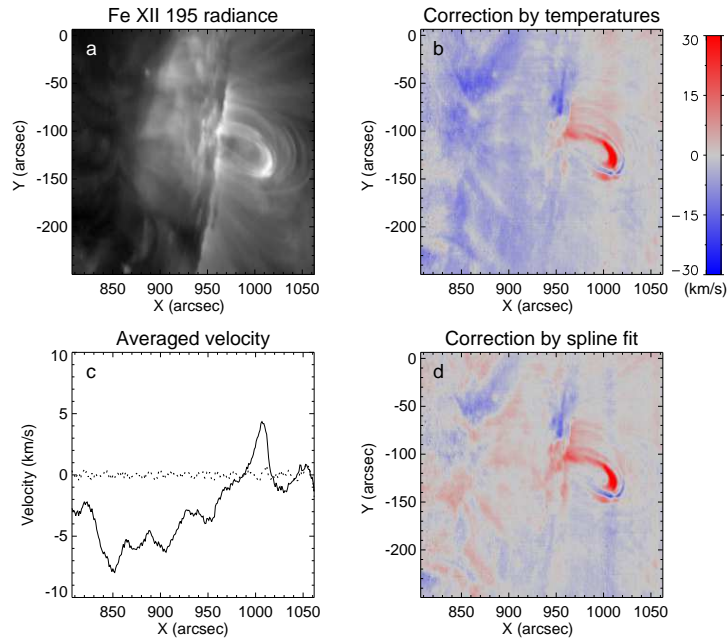


Figure 6. Coronal loops observed after a flare at the West limb on 17 Dec 2006. a: The emission in Fe XII $\lambda 195.12 \text{ \AA}$ displayed in log scale. b: Doppler velocity derived from Fe XII $\lambda 195.12 \text{ \AA}$ after correction in the present paper. c: Profiles of averaged velocity at each exposure. Solid line and dotted line indicate resultant velocity after correction by the method in the present paper and the spline fit. d: Doppler velocity after subtracting spline fit to the observed spectral position.

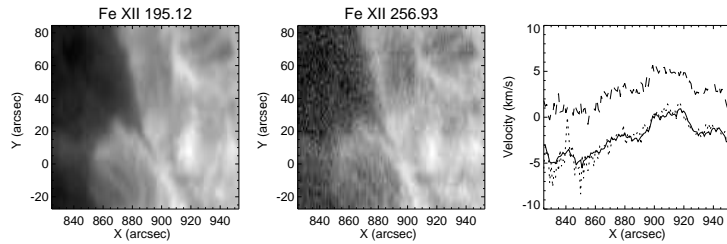


Figure 7. Left: A cut-out of an active region observed on 24 May 2007. The emission in Fe XII $\lambda 195.12 \text{ \AA}$ is displayed in log scale. Middle: The emission in Fe XII $\lambda 256.93 \text{ \AA}$. Right: Solid line and dotted line respectively show averaged Doppler velocities at each exposure in Fe XII $\lambda 195.12 \text{ \AA}$ and in Fe XII $\lambda 256.93 \text{ \AA}$. Dashed line indicates the velocity for Fe XI $\lambda 180.40 \text{ \AA}$, which is shifted by $+5 \text{ km s}^{-1}$ to avoid overlap.

other wavelengths. The validity of our correction method is examined by using Fe XII $\lambda 195.12 \text{ \AA}$ in the short wavelength band and Fe XII $\lambda 256.93 \text{ \AA}$ in the long wavelength band. As the two lines are emitted from the same type of ion, they must indicate identical Doppler velocities. These two lines allow us to assess if the correction method derived from the short wavelength band can be also applied to the long wavelength band.

Figure 7 shows a part of an active region observed in Fe XII $\lambda 195.12 \text{ \AA}$ and $\lambda 256.93 \text{ \AA}$ on 24 May 2007. Correction of the spectral drift is mandatory because it took 60 min to complete the raster scan. To compare the two emission lines, a spatial offset along the EIS slit must be corrected, which is about 16 arcsec in the north – south direction (see Appendix B for the spatial offset of the spectrum). Then the estimated spectral drift on the detector is subtracted from both lines. It must be noted that the instrumental spectral shifts are not in the velocity scale but in the detector pixel scale, because the velocity scale varies with wavelength; Doppler velocities corresponding to one pixel width of the detector are 34 km s^{-1} at $\lambda 195.12 \text{ \AA}$ and 26 km s^{-1} at $\lambda 256.93 \text{ \AA}$. Two panels in Figure 7 present radiance maps after correcting the spatial offset. They show quite similar structure in the active region, although Fe XII $\lambda 256.93 \text{ \AA}$ appears noisier because of its low emission. Averaged Doppler velocities at each exposure is plotted in the right panel of Figure 7. The velocities inferred from two Fe XII lines are in good agreement, which proves that our method of spectral drift correction can be applied to the long wavelength band as well as to the short wavelength band. An increased deviation in the left part of the plot is due to a large uncertainty caused by a low emission in Fe XII $\lambda 256.93 \text{ \AA}$. In addition, the velocity derived from Fe XI $\lambda 180.40 \text{ \AA}$ is displayed in the right panel with $+5 \text{ km s}^{-1}$ offset. Although it is emitted from a different ionization level, the velocity profile is more or less the same as those of Fe XII emission lines.

4. Discussion

We constructed an empirical method to compensate for the spectral drift from instrumental temperature changes and the motion of the spacecraft. It consists of three different ANNs to accommodate discontinuities in spectral positions. The composite model reproduces observed spectral drift with moderate accuracy; rms of the residual is 0.13 pixel or 4.4 km s^{-1} at Fe XII $\lambda 195.12 \text{ \AA}$. The results demonstrate that the spectral drift of two-pixel amplitude is effectively suppressed by this method, which proves that the main cause of spectral shift is temperature variations in the spectrometer and relative motion of the spacecraft.

Incompleteness of the model is considered as a cause of the residuals between the actual spectral positions and the estimations. Although the ANNs are built from 34 temperature inputs, they may not be sufficient to represent the temperature distribution of the spectrometer completely. In addition, short exposure data are incorporated for the sake of a better coverage of observing period, which has a large uncertainty in spectral position because of low counts. Considering that the accuracy of a Gaussian fit is roughly 0.1 pixel for a typical spectrum recorded by EIS, the performance of 0.13 pixel uncertainty is reasonable.

Another possible cause of the error is due to flows in the solar corona. Even though the spectral positions are averaged over 240 arcsec of the slit, high speed flows in active regions could alter the spectral position. However, the majority of spectra have been obtained in quiet regions because of the low solar activity in 2006 – 2009. Thus, active regions affect only a small fraction of the data.

As the ANN is optimized to minimize the discrepancy between the model estimate and measured spectral position, it assumes that mean velocity of the

entire data set is zero. Since the large number of data sets used in building the model virtually covers the entire Sun, the velocity origin should be adjusted to the global average of the Fe XII $\lambda 195.12 \text{ \AA}$ emission line. It has been reported in the literature that the net velocity of coronal emission lines deviates from zero (Peter and Judge, 1999; Teriaca, Banerjee, and Doyle, 1999). Peter and Judge (1999) determined a net blueshift of $4.5 \pm 1.3 \text{ km s}^{-1}$ in Mg X formed at 10^6 K at the disk center. Teriaca, Banerjee, and Doyle (1999) found a blueshift of $9.8 \pm 1.6 \text{ km s}^{-1}$ in Fe XII $\lambda 1242.0 \text{ \AA}$ in an active region. If net upflow exists in the corona, observed spectra should exhibit a center to limb variation of the Doppler shift, which could partly account for the uncertainty of our velocity correction method. However, a comparison between mean velocities at the disk center and at the limb in our data indicates no significant difference. It is fair to claim the amount of center to limb variation is within the uncertainty of the correction method or 4.4 km s^{-1} , as this correction method may not be accurate enough to measure a small velocity.

The velocity calibration method developed in the present paper is suitable for active region studies, as it does not require a velocity reference in the observing field. A commonly used method so far is to assume that the average velocity at each slit position is zero. But the mean velocity in active regions may deviate from zero since localized high speed flows are frequently observed. For example, the coronal loops in Figure 6 exhibits a significant Doppler shift of about 40 km s^{-1} , which was interpreted as siphon flow along the loops (Hara *et al.*, 2008). Hara *et al.* (2008) found a steady outflow up to 50 km s^{-1} in the periphery of an active region, where magnetic fields extend to the outer corona. A 15 km s^{-1} blueshift found at around $X = 850$ in Figure 6 could be interpreted as an outflow in the vicinity of the active region. The correction by the zero velocity assumption could be improved by carefully selecting a quiet region in the observing field, but a quiet region is not always available in active region observations. The advantage of our method is that it does not rely on the mean velocity in the observing field and is applicable to any observations with the EIS.

5. Conclusions

An empirical method for velocity calibration is constructed using data from three years of observations with the EIS. It estimates instrumental spectral drift from temperatures inside the spectrometer and relative motion of the spacecraft. The model reproduces observed spectral position on the detector with a moderate accuracy of 0.13 pixel or 4.4 km s^{-1} at the Fe XII $\lambda 195.12 \text{ \AA}$ emission line. It proves that the spectral drift, which introduces difficulties in velocity measurement with EIS, is primarily caused by temperature variations inside the spectrometer. This model works in the eclipse period, when the spacecraft experiences severe temperature variation in the day – night cycle, as well as in the day period.

Since our new method requires only spacecraft status data, it is applicable to any spectrum recorded by the EIS. It can be applied to both the short and the

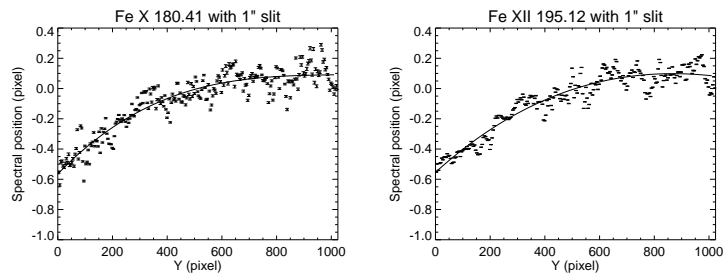


Figure 8. Spectrum center position determined from Fe x $\lambda 180.41 \text{ \AA}$ and Fe XII $\lambda 195.12 \text{ \AA}$ in the short wavelength band. Positions are in pixel unit with respect to the detector center ($Y=512$). Solid line presents the fitted third order polynomial function.

long wavelength bands, as the instrumental effect produces the same amount of spectral drift in the entire wavelength range of the EIS. The correction method would be particularly useful for active region and flare observations since no velocity reference is needed. This procedure is provided as a part of the SSW.

Appendix

A. Spectral Curvatures of EIS

Spectral curvatures on the detector are determined by using long exposure data in quiet regions. Correction of the curvatures is crucial for a precise Doppler shift measurement with the EIS. We selected two data sets recorded in a quiet region at disk center; the first light of the EIS on 28 October 2006 and the velocity calibration data on 26 November 2009.

To cover the 1024-pixel height of the EIS detector, two exposures in the top and bottom halves of the CCD are required, since only a 512-pixel height can be read out at one time. Another exposure in the middle of detector is needed to bridge them because temperature variation of the spectrometer causes instrumental spectral drift in the wavelength dimension between the two exposures (see main text for details). The central position of the spectrum was determined by fitting a Gaussian function at each slit height. Fe x $\lambda 180.41 \text{ \AA}$, Fe XII $\lambda 195.12 \text{ \AA}$, Fe x $\lambda 257.28 \text{ \AA}$, and S x $\lambda 264.23 \text{ \AA}$ are selected as they provided good count statistics and were not affected by blending lines. The spectral drifts between the three exposures were determined by comparing averaged spectral positions in overlapping regions. The averaged velocities of common region were assumed to be unchanged, although these spectra were recorded at different times. Spectra in the top and bottom halves were combined after compensating the spectral drifts.

Figure 8 presents spectral center positions derived from the short wavelength band data on 26 October 2006. In order to smooth out small scale fluctuations, they are fitted by a third order polynomial function. The functions fitted to Fe x $\lambda 180.41 \text{ \AA}$ and Fe XII $\lambda 195.12 \text{ \AA}$ are quite similar and their difference is below

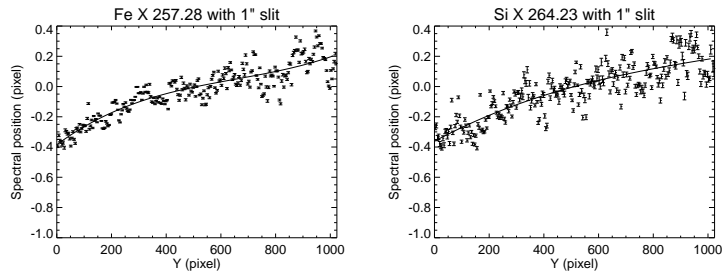


Figure 9. The same as Figure 8 but for Fe x $\lambda 257.28 \text{ \AA}$ and S x $\lambda 264.23 \text{ \AA}$ in the long wavelength band.

the uncertainty of the fitted functions. It implies that the spectral curvatures are the same within the short wavelength band.

Similarly, spectral curvatures in the long wavelength band are determined from Fe x $\lambda 257.28 \text{ \AA}$ and S x $\lambda 264.23 \text{ \AA}$ (Figure 9). Two spectral lines show very similar curvatures though they are different from those of the short wavelength band. To study the spectral curvatures in both wavelength bands of EIS, at least one spectral line for each band must be analyzed. In the following study, Fe XII $\lambda 195.12 \text{ \AA}$ in the short wavelength band and Fe x $\lambda 257.28 \text{ \AA}$ in the long wavelength band are analyzed since these lines had better count statistics than others.

Figures 10a and 10b present functions fitted to spectra on 28 October 2006. The long and the short wavelength bands show different functions as mentioned above. The $2''$ width slit has larger tilt with respect to the detector than the $1''$ width slit and causes a large linear slope of the spectrum. Spectral curvatures on 26 November 2009 show quite different characteristics (Figures 10c and 10d). Compared to 28 October 2006 in Figures 10a and 10b, the tilt of both slits increased in the short wavelength band, while they decreased in the long wavelength band.

A possible cause of the spectral curvature change is movement of the slit and the grating during the period. Figures 10e and 10f present offlimb spectra before and after the slit focus adjustment on 24 August 2008. Although it covers only $512''$ height along the slit, the effect of the the slit focus adjustment can be assessed by comparing them. In Figure 10e before the slit adjustment, spectral positions fall on the solid line of 28 October 2006. After the slit adjustment (in Figure 10f), it fits well on the dashed line of 26 November 2009. The results suggest that the slit focus movement on 24 August 2008 is the primary cause of spectral curvature change. Although the grating was moved on 21 October 2008, it seems only to have a minor impact on spectral curvatures. No other movement of the optical element of the EIS has been done by the time this article was written.

Parameters for the fitted functions are summarized in Table 2. The spectral shift s at given slit height is expressed as

$$s = c_0 + c_1 y + c_2 y^2 + c_3 y^3 \quad (1)$$

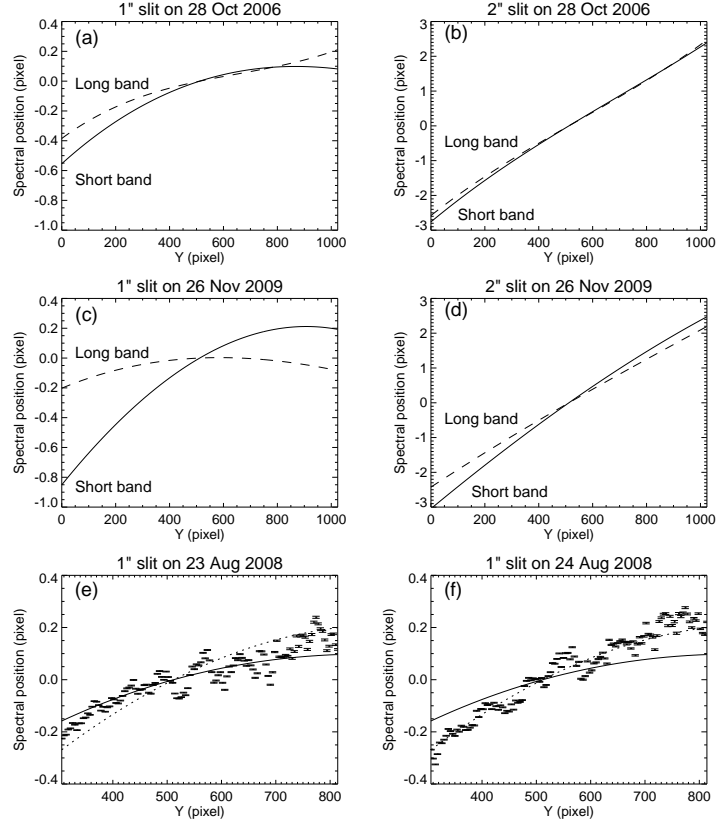


Figure 10. Variation of the EIS spectral curvature. a: spectral curvatures with 1'' width slit on 28 October 2006. Solid line and dashed line respectively indicate the third order polynomial functions fitted to Fe XII $\lambda 195.12 \text{ \AA}$ in the short wavelength band and Fe X $\lambda 257.28 \text{ \AA}$ in the long wavelength band. Positions are adjusted to zero at the detector center ($Y=512$). b: the same as a but for 2'' width slit. c and d: the same format as a and b but for 26 November 2009. e: spectral positions of Fe XII $\lambda 195.12 \text{ \AA}$ on 23 August 2008, before the slit focus adjustment. Solid and dotted lines indicate spectral curvatures on 28 October 2006 and 26 November 2009, respectively. f: the same as e but for 24 August 2008, after the slit focus adjustment.

Table 2. Fitted parameters for spectral curvatures

Date	Slit	Band	c_0	c_1	c_2	c_3
28 Oct 2006	1''	short	-0.55	1.63×10^{-3}	-1.17×10^{-6}	1.73×10^{-10}
		long	-0.38	1.33×10^{-3}	-1.54×10^{-6}	7.87×10^{-10}
	2''	short	-2.76	6.44×10^{-3}	-2.71×10^{-6}	1.30×10^{-9}
		long	-2.58	6.15×10^{-3}	-3.15×10^{-6}	1.92×10^{-9}
26 Nov 2009	1''	short	-0.84	2.19×10^{-3}	-9.76×10^{-7}	-1.75×10^{-10}
		long	-0.18	7.39×10^{-4}	-9.00×10^{-7}	2.94×10^{-10}
	2''	short	-3.04	6.40×10^{-3}	-8.01×10^{-7}	-1.88×10^{-10}
		long	-2.42	5.08×10^{-3}	-7.94×10^{-7}	2.32×10^{-10}

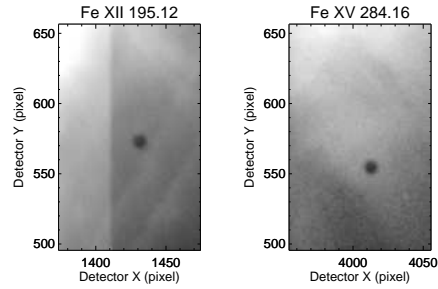


Figure 11. Left: Mercury transit seen in Fe XII $\lambda 195.12 \text{ \AA}$ emission, displayed in log scale. Axis indicate dimensions in CCD pixel. Right: Emission in Fe XV $\lambda 284.16 \text{ \AA}$.

where y is a position in CCD pixel coordinates. Before the slit adjustment on 24 August 2008, spectral curvatures can be corrected by using the parameters fitted to spectra on 28 October 2006. After the slit adjustment, the spectral curvatures can be compensated for by using another set of parameters fitted to spectra on 26 November 2009.

B. Spatial Offset of the Spectrum

Because of the tilt of the grating with respect to the detector, spectra recorded by EIS have a wavelength dependent offset in the north – south direction (Young *et al.*, 2009). To compare multiple emissions from the same feature of the Sun, it is essential to correct the spatial offset along the slit. The Mercury transit observed by the EIS on 8 November 2006 provided a unique opportunity to determine the spatial offset. Since the solar emission is obscured by Mercury, a shadow must be seen at identical locations in all wavelengths. By using the EIS slot observing mode, two dimensional images in strong emission lines were recorded. The spatial offset is determined by measuring the positions of the Mercury shadow in selected emission lines.

Figure 11 shows images during the Mercury transit in Fe XII $\lambda 195.12 \text{ \AA}$ and Fe XV $\lambda 284.16 \text{ \AA}$, which were obtained at 18:52 UTC by the $266''$ -wide slot. Mercury produced a round shadow against a bright emission from the solar corona. The apparent diameter of Mercury was about 10 pixel on the detector, where the plate scale is $1'' \text{ pixel}^{-1}$. Other images were obtained with the $40''$ -wide slot later at 21:30 UTC. Since two dimensional images obtained with the EIS slots are overlapping with nearby emission lines, prominent emission lines are selected for this study, namely; Fe XI $\lambda 181.23 \text{ \AA}$, Fe XII $\lambda 193.51 \text{ \AA}$, Fe XII $\lambda 195.12 \text{ \AA}$, Fe XIII $\lambda 202.04 \text{ \AA}$, He II $\lambda 256.32 \text{ \AA}$, Fe XIV $\lambda 264.79 \text{ \AA}$, Fe XIV $\lambda 274.20 \text{ \AA}$, and Fe XV $\lambda 284.16 \text{ \AA}$. The $40''$ slot observations allowed measurements in more lines than did the $266''$ slot as the overlap of emission lines is limited. The position of Mercury at each emission line is determined by measuring the centroid of the shadow profile in the north – south direction. The estimated accuracy of the shadow position measurement is 0.3 pixel.

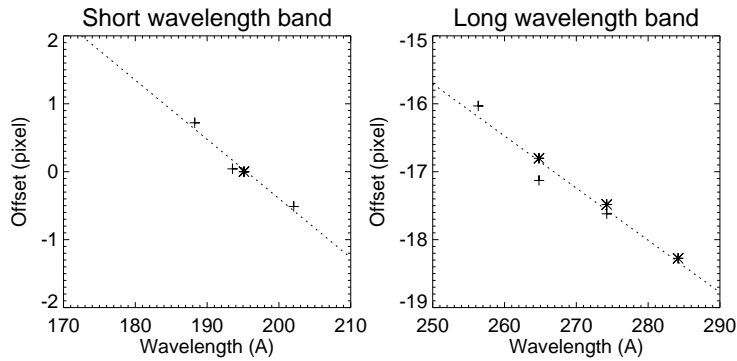


Figure 12. Left: Spatial offsets measured in the short wavelength band from the Mercury transit on 8 November 2006. Plus and asterisk signs indicate offsets deduced from $40''$ -wide slot and $266''$ -wide slot images of the EIS. The offset at $\text{Fe XII } \lambda 195.12 \text{ \AA}$ is adjusted to zero. Right: Spatial offsets in the long wavelength band with respect to $\text{Fe XII } \lambda 195.12 \text{ \AA}$.

Figure 12 presents spatial offsets measured at different wavelength. Measurements from the $40''$ and $266''$ wide slots give a consistent spatial offset. A linear function fitted to the short wavelength band is expressed as

$$y = -8.72 \times 10^{-2} \lambda + 17.01 \quad (2)$$

where λ is the wavelength in \AA . Young *et al.* (2009) determined a gradient of -7.92×10^{-2} in the short wavelength band. Their value is consistent with our result since the discrepancy within the commonly used range of 180 \AA to 203 \AA is only 0.18 pixel, which is close to the uncertainty of the offset measurement. The spatial offset for the long wavelength band is determined in the same manner.

$$y = -7.68 \times 10^{-2} \lambda + 3.49 \quad (3)$$

The spatial offset in both wavelength bands of the EIS can be compensated for by using the plate scale of $1.002 \pm 0.016 \text{ arcsec pixel}^{-1}$ (Hara, 2008) and equations (2) and (3). In addition, Hara (2008) also determined the normal scan step size of $0.961 \pm 0.004 \text{ arcsec}$, which can be used to deduce the width of a raster scan in east – west direction.

Acknowledgements *Hinode* is a Japanese mission developed and launched by ISAS/JAXA, with NAOJ as domestic partner and NASA and STFC (UK) as international partners. It is operated by these agencies in co-operation with ESA and NSC (Norway). Authors are grateful to the ROOT development team for providing a useful software package. We would like to thank Dr. J. M. Borrero for fruitful discussion on developing artificial neural network.

References

- Bishop, C.M.: 1995, *Neural networks for pattern recognition*, Oxford University Press, Oxford.
 Borrero, J.M., Tomczyk, S., Kubo, M., Socas-Navarro, H., Schou, J., Couvidat, S., Bogart, R.: 2010, *Solar Phys.*, in press.
 Brown, C.M., Hara, H., Kamio, S., Feldman, U., Seely, J.F., Doschek, G.A., *et al.*: 2007, *Publ. Astron. Soc. Japan* **59**, 865.

-
- Brun, R., Rademakers, F.: 1997, *Nucl. Inst. Methods. in Phys. Res.* **389**, 81.
- Carroll, T.A., Staude, J.: 2001, *Astron. Astrophys.* **378**, 316.
- Culhane, J.L., Harra, L.K., James, A.M., Al-Janabi, K., Bradley, L.J., Chaudry, R.A., *et al.*: 2007, *Solar Phys.* **243**, 19.
- Hara, H.: 2008, In: Matthews, S. A., Davis, J. M., & Harra, L. K. (eds.) *First Results From Hinode, ASP Conf. Ser.* **397**, 11.
- Hara, H., Watanabe, T., Matsuzaki, K., Harra, L.K., Culhane, J.L., Cargill, P., Mariska, J.T., Doschek, G.A.: 2008, *Publ. Astron. Soc. Japan* **60**, 275.
- Harra, L.K., Sakao, T., Mandrini, C.H., Hara, H., Imada, S., Young, P.R., van Driel-Gesztelyi, L., Baker, D.: 2008, *Astrophys. J. Lett.* **676**, 147.
- Korendyke, C.M., Brown, C.M., Thomas, R.J., Keyser, C., Davila, J., Hagood, R., *et al.*: 2006, *Appl. Opt.* **45**, 8674.
- Kosugi, T., Matsuzaki, K., Sakao, T., Shimizu, T., Sone, Y., Tachikawa, S., *et al.*: 2007, *Solar Phys.* **243**, 3.
- Lang, J., Kent, B.J., Paustian, W., Brown, C.M., Keyser, C., Anderson, M.R., *et al.*: 2006, *Appl. Opt.* **45**, 8689.
- Matsuzaki, K., Shimojo, M., Tarbell, T.D., Harra, L.K., Deluca, E.E.: 2007, *Solar Phys.* **243**, 87.
- Peter, H., Judge, P.G.: 1999, *Astrophys. J.* **522**, 1148.
- Rybák, J., Curdt, W., Kucera, A., Schühle, U., Wöhl, H.: 1999, In: Wilson, A. (ed.) *Magnetic Fields and Solar Processes, ESA SP-448*, 361.
- Socas-Navarro, H.: 2003, *Neural Networks* **16**, 355.
- Teriaca, L., Banerjee, D., Doyle, J.G.: 1999, *Astron. Astrophys.* **349**, 636.
- Tsuneta, S., Ichimoto, K., Katsukawa, Y., Nagata, S., Otsubo, M., Shimizu, T., *et al.*: 2008, *Solar Phys.* **249**, 167.
- Young, P.R., Watanabe, T., Hara, H., Mariska, J.T.: 2009, *Astron. Astrophys.* **495**, 587.